JOURNAL OF MATERIALS SCIENCE **34** (1999) 4921–4929

The crack tip strain field of AISI 4340

Part II *Experimental measurements*

N. N. KINAEV[‡§], D. R. COUSENS[§], A. ATRENS[‡*]
[‡]*Department of Mining, Minerals and Materials Engineering, The University of Queensland, Brisbane, QLD, 4072*
[§]*Centre for Microscopy and Microanalysis, The University of Queensland, QLD, 4072*
E-mail: atrens@minmet.uq.oz.au

Crack tip strain maps have been measured for AISI 4340 high strength steel. No significant creep was observed. The measured values of CTOD were greater than expected from the HRR model. Crack tip branching was observed in every experiment. The direction of crack branching was in the same direction as a major "ridge" of ε_{yy} strain, which in turn was in the same direction as predicted by the HRR model. Furthermore, the measured magnitudes of the ε_{yy} strain in this same direction were in general greater than the values predicted by the HRR model. This indicates more plasticity in the crack tip region than expected from the HRR model. This greater plasticity could be related to the larger than expected CTOD values. The following discrepancies between the measured strain fields for AISI 4340 and the HRR predictions are noteworthy: (1) The crack branching. (2) Values of CTOD significantly higher than predicted by HRR. (3) The major "ridge" of ε_{yy} strain an angle of about 60° with the direction of overall propagation of the fatigue precrack, in which the measured magnitudes of the ε_{yy} strain were greater than the values predicted by the HRR model. (4) Asymmetric shape of the plastic zone as measured by the ε_{yy} strain. (5) Values of shear strain γ_{xy} significantly higher than predicted by the HRR model.

1. Introduction

This paper is the second of a series of papers describing a study which has measured the crack tip strain field for AISI 4340 high strength steel. Kinaev *et al.* [1] in Part I described the measurement technique. This present paper presents the crack tip strain measurements using specimens loaded in high vacuum and therefore represents measurement of the intrinsic strain field with no environmental influence. Kinaev *et al.* [2] in Part III describe the experimental results obtained in the presence of pure hydrogen and water vapour. This present study builds on our prior work [3–6] which has shown that stress rate effects can be an important part of the SCC mechanism for high strength steels undergoing SCC in water. In particular, Oehlert and Atrens [6] showed that high strength steels like 4340 do undergo a significant amount of primary creep at room temperature. The present study was undertaken to measure creep effects at the crack tip in order to relate crack tip plasticity to stress corrosion cracking. As part of this overall aim, the crack tip strain field has been measured and is compared with theoretical expectations.

There are several theoretical models which describe the strain distribution at the crack tip. The most developed model is that due to Hutchinson-Rice-Rosengren (HRR) [7–9]. The HRR model describes stress and strain fields at the crack tip for a strain hardening material that is isotropic and homogeneous. In the crack-tip region, the elastic strains are small compared to the plastic strains and can be neglected. Therefore, only the plastic stresses and strains are considered. The material is assumed to satisfy a power law relation between stress and strain of the type:

$$\frac{\varepsilon}{\varepsilon_0} = \alpha\left(\frac{\sigma}{\sigma_0}\right)^n \tag{1}$$

where ε and σ are the uniaxial plastic strain and stress, σ_0 is the yield stress, $\varepsilon_0 = \sigma_0/E$ is the yield strain, E is Young's modulus, α is a material constant and n is the strain hardening exponent.

In polar coordinates (angle θ and radial distance from the crack tip ρ) the asymptotic crack tip strain is [7–9]

$$\varepsilon_{ij} = \alpha\left[\frac{J}{\alpha\sigma_0\varepsilon_0 I_n \rho}\right]^{\frac{n}{n+1}} \tilde{\varepsilon}_{ij}(\theta, n) \tag{2}$$

where i, j correspond to the radius ρ and angle θ in polar coordinates, ε_{ij} is a corresponding strain (e.g. $\varepsilon_{\rho\rho}$, $\varepsilon_{\theta\theta}$, $\varepsilon_{\rho\theta}$), J is the J integral, n is the strain hardening exponent, I_n is a dimensionless constant, ρ is the distance

* Author to whom all correspondence should be addressed.

from the crack tip, and $\tilde{\varepsilon}_{ij}(\Theta, n)$ is the θ-variation which also depends on n and plane stress/plane strain conditions and is given in tabular form by Shih [10].

The strains in polar coordinates can be converted into the Cartesian coordinates using the transformations:

$$\begin{cases} \varepsilon_{xx} = \varepsilon_{\rho\rho}\cos^2(\theta) + \varepsilon_{\theta\theta}\sin^2(\theta) - 2\sin(\theta)\cos(\theta)\varepsilon_{\rho\theta} \\ \varepsilon_{yy} = \varepsilon_{\rho\rho}\sin^2(\theta) + \varepsilon_{\theta\theta}\cos^2(\theta) - 2\sin(\theta)\cos(\theta)\varepsilon_{\rho\theta} \\ \gamma_{xy} = (\varepsilon_{\rho\rho} - \varepsilon_{\theta\theta})\sin(\theta)\cos(\theta) \\ \quad + (\cos^2(\theta) - \sin^2(\theta))\varepsilon_{\rho\theta} \end{cases} \quad (3)$$

The crack tip opening displacement CTOD is given [10] by the HRR model as

$$\text{CTOD} = (\alpha\varepsilon_0)^{1/n} D_n \frac{J}{\sigma_0} \quad (4)$$

where D_n is a dimensionless coefficient. The HRR model neglects deformation-induced geometry changes such as crack tip blunting.

A number of the experimental determination of the crack tip strain distribution [11–13] have been previously carried out in which the size of the plastic zone was of the order of several mm. In these studies, the crack tip strain fields have been in relatively good agreement with the HRR model. However, there have been no experimental examinations of the applicability of the HRR model when the plastic zone size is of the order of 50 μm. Plastic zones of this size are present in high strength steels like 4340 and consequently, it is important to test the applicability of the HRR model to this important category of engineering materials.

2. Experimental

The material used in this study was AISI 4340 high strength steel. The chemical composition is given in Table I. The steel was austenitised at 870 °C for 3 h followed by quenching into agitated oil. The grain size of the material was 3–5 μm. After heat treatment the yield stress was 1670 MPa and hardness was in the range of 50–55 HRC.

A bolt-loaded DCB sample geometry as described by [1] was used in all experiments. Fatigue pre-cracking was carried out at a frequency of 50 Hz with an applied stress intensity factor cycling between a slightly positive value and a maximum value in the range of $\leq$12 MPa $\sqrt{\text{m}}$, so that $\Delta K \leq 7$ MPa $\sqrt{\text{m}}$. The sample was loaded inside the ESEM "Electroscan—E3" in high vacuum accordingly to the procedure described previously [1]. The samples were held in high vacuum ($\sim 10^{-5}$ torr) for 2 h before loading to minimise possible effects of residual water vapour in the ESEM. The loading corresponded to stress intensities factors of 15, 20, 25, and 35 MPa $\sqrt{\text{m}}$; a new specimen was used at each value of the stress intensity factor. Images were captured in each case 1 (or 2), 5, 10, 15, 30, 45, and 60 min after loading. The images were processed and the positions of reference points were measured accordingly to the procedure described in [1] with an accuracy of ± 0.25 to ± 0.5 μm, depending on the contrast of the captured image.

Strain values (ε_{xx}, ε_{yy}, and γ_{xy}) were calculated using a modified version of the algorithm of Allais *et al.* [14] as described by Kinaev *et al.* [1]. The error analysis [1] indicated that reliable strain could be obtained for distances greater than 4 μm from the crack tip. The minimum measurable strain was 0.02. Thus, only plastic strains could be measured, as there was insufficient precision for elastic strain determination.

The total effective strain ε_{ef} was calculated accordingly to the following equation [15]:

$$\varepsilon_{\text{ef}} = \frac{2}{3} \cdot \sqrt{\varepsilon_1^2 + \varepsilon_1\varepsilon_2 + \varepsilon_2^2} \quad (5)$$

where ε_1 and ε_2 are the principal strains, which were calculated from ε_{xx}, ε_{yy}, and γ_{xy} using [16]:

$$\varepsilon_{1,2} = \frac{1}{2}\left(\varepsilon_{xx} + \varepsilon_{yy} \pm \sqrt{((\varepsilon_{xx} - \varepsilon_{yy})^2 + \gamma_{xy}^2)}\right) \quad (6)$$

The total effective strain is a parameter representing the directionless absolute magnitude of the strain tensor or, in other words, a measure of the total deformation that occurred at a particular point.

The experimental strain maps presented in this paper are compared with the predictions of the HRR model. The strain hardening exponent n ($n = 1.9$) and the material constant α ($\alpha = 2450$) were determined experimentally from tensile stress-strain curves obtained from the same material (AISI 4340 steel) subjected to the same heat treatment. The dimensionless constant I_n and the θ-variations for $\tilde{\varepsilon}_{ij}(\theta, n)$ for plane stress were taken from Shih [10]. The length of the crack was in each case significantly larger than the size of the plastic zone, and thus, the small scale yielding criteria was satisfied. Thus it was possible to estimate the value of J integral with the equation

$$J = \frac{K_I^2}{E} \quad (7)$$

The experimental strain distributions were averaged over the time sequence for every stress intensity factor considered (15, 20, 25, and 35 MPa $\sqrt{\text{m}}$), except for those presented in Section 3.4.

TABLE I Chemical composition of the AISI 4340 steel (%)

C	Mn	Si	S	P	Ni	Cr	Mo	Cu	V	Al
.09	.86	.27	.005	.016	.70	.45	.39	.21	.03	.061

3. Results

3.1. Crack front profile

After the strain measurements, the samples were heated to 150 °C in air to thermally mark the crack front and broken open using the "Instron" hydraulic testing machine. The crack front profiles, determined using

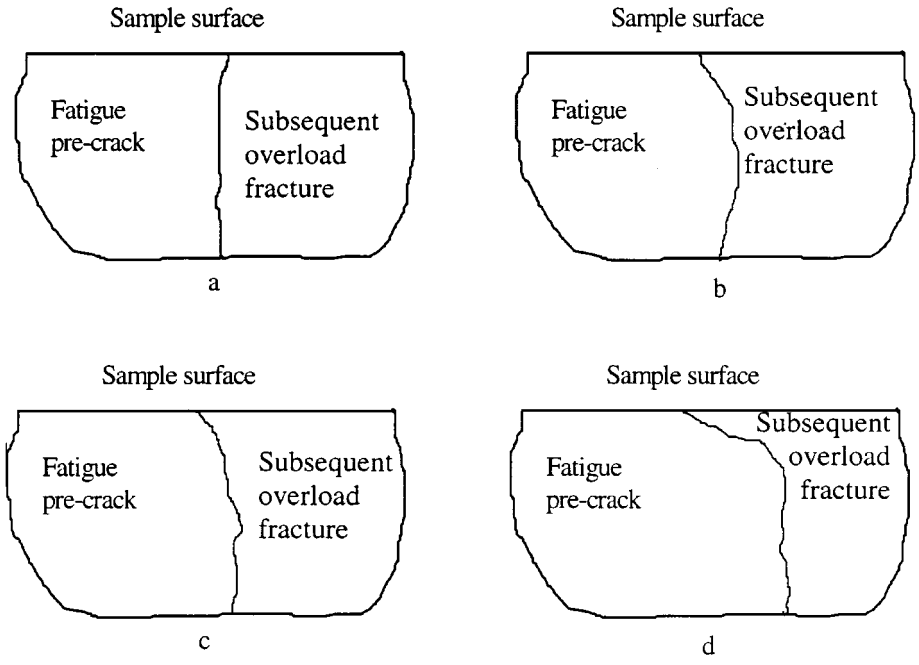

Figure 1 Shape of the fatigue pre-crack profile as visible on the fracture surface after breaking the specimen open after the experiments for the following values of stress intensity factor K_I (a) 35 MPa $\sqrt{\text{m}}$; (b) 25 MPa $\sqrt{\text{m}}$; (c) 20 MPa $\sqrt{\text{m}}$; (d) 15 MPa $\sqrt{\text{m}}$.

optical microscopy, are presented in Fig. 1. In this figure, the "sample surface" corresponds to the surface from which the strain fields were determined. As illustrated in Fig. 1, in all the experiments except the one at an applied stress intensity factor K_I of 35 MPa $\sqrt{\text{m}}$ (Fig. 1a), the fatigue pre-crack in the sample interior was longer than at the surface. This deviation from the ideal straight crack front could introduce some deviations from the theoretical predictions. However, for the experiment at the highest applied stress intensity factor of K_I of 35 MPa $\sqrt{\text{m}}$, the crack front profile was close to the ideal shape, perpendicular to the observed sample surface. Thus most emphasis for the comparison of the experiments with the theory was placed on the experiments at an applied stress intensity factor of K_I of 35 MPa $\sqrt{\text{m}}$, where the crack front profile was close to ideal.

3.2. Crack tip shape

The shape of the crack tip is shown in Fig. 2 for each of the four experimental loading conditions. There was significant crack tip branching in all cases. The direction of the crack tip branching made an angle of about 60° with the direction of crack propagation. The experimental apparatus did not permit imaging of the sample during loading, and hence no information was available concerning the kinetics of crack tip branching. It was not possible to determine whether the crack tip started to branch during the loading or as a result of creep occurring within the first minute after the loading. The mechanism of crack tip branching is unclear.

One possibility is that the crack extended during loading in both directions of the maximum σ_{yy} stress/ε_{yy} strain, followed by preferential growth in one of these two directions. The preference of one of these directions could be a result of slight deviations from symmetry for the loading and/or microstructural variations.

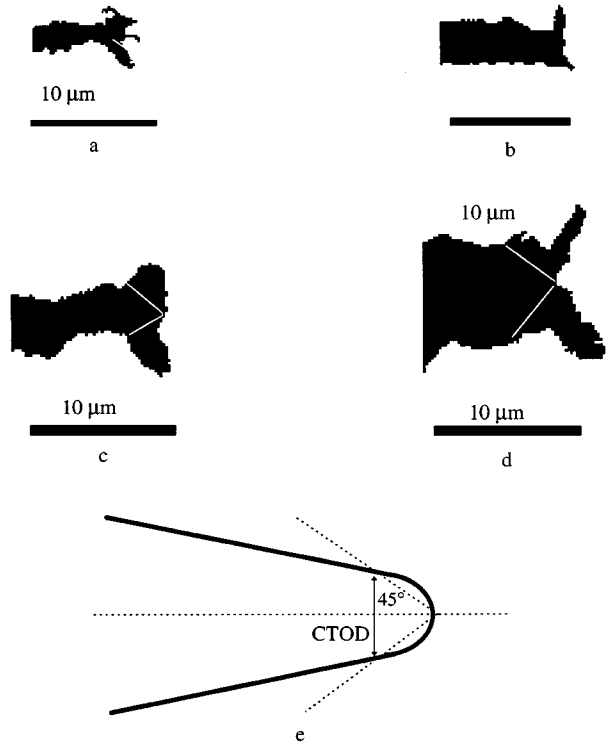

Figure 2 Cross-sectional shape of the crack tip for the following values of the stress intensity factor K_I (a) 15 MPa $\sqrt{\text{m}}$; (b) 20 MPa $\sqrt{\text{m}}$; (c) 25 MPa $\sqrt{\text{m}}$; (d) 35 MPa $\sqrt{\text{m}}$. In each case the scale bar is equal to 10 μm; (e) definition of the crack tip opening displacement in HRR model.

Alternatively, crack tip branching might occur due to creep occurring within the first minute after loading. In this case the plastic deformations leading to the crack tip branching would be expected to occur in the directions of maximum ε_{yy} strain. The microstructural characteristics of a material in a vicinity of a crack tip are not necessarily symmetric. Therefore, creep and crack extension could developed preferentially in one of the two possible directions.

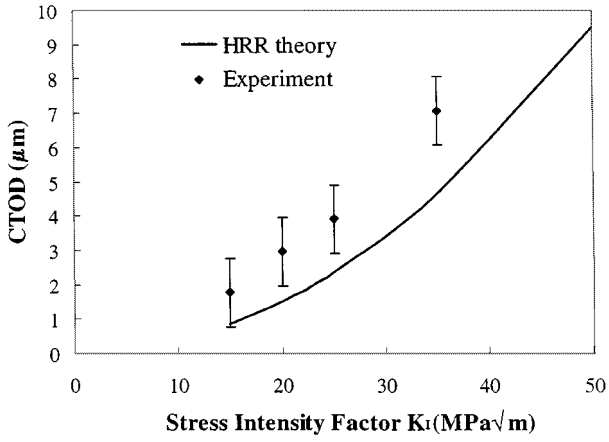

Figure 3 Comparison of the experimental values of CTOD with the ones predicted by HRR model.

The asymmetry of the crack tip could be the result of even a slight asymmetry in the stress distribution. Alternatively the major factor responsible for the crack tip asymmetry could be the non symmetrical plastic response of the material in the vicinity of the crack tip to a symmetrical stress distribution.

3.3. Crack tip opening displacement

The crack tip opening displacement (CTOD) was evaluated from the definition of CTOD as given in the HRR model as illustrated in Fig. 2e. The results are presented in Fig. 3, where the experimental values are compared with the theoretical values of CTOD calculated using Equation 4. The experimental values of CTOD were higher than the HRR predictions although the general trend was consistent with the theoretical predictions. Some of the higher value of the experimental results compared with the HRR model might be related to the additional plastic deformation at the crack tip due to the crack branching.

3.4. Time dependence of strain

Examples of the time variation of the ε_{yy} strain distribution for experiments with an applied stress intensity factor of 35 MPa $\sqrt{\text{m}}$ are presented in Fig. 4. This figure shows that over most of the strain field there was no statistically significant change of the strain distribution with time. Similarly, at each of the other applied stress intensity factors, there was little statistically significant change in ε_{yy} with time over the period from 1 to 60 min. This absence of creep could have three explanations: (1) creep did not occur at all; (2) the changes due to creep were smaller than the measurement accuracy (± 0.02); or (3) creep occurred so fast that the major changes happened within the first minute after loading. The second possibility must be considered probable as the prior measurements by Oehlert and Atrens [6] indicated small values (less than 0.001) for the primary creep strain at room temperature for smooth specimens at stresses below the yield stress.

The absence of statistically meaningful creep indicated that it was valid to calculate average strain maps for each time series, and such average strain maps are used throughout the rest of this paper. The average strain of the each time series at each data point was calculated using: $\bar{\varepsilon} = \frac{1}{n}\sum_{i=1}^{n}\varepsilon_i$, where ε_i was the strain for the ith measurement and $n = 7$ was the number of the strain distributions measured at the different times. The maximum standard deviation of the strain values through the time series was slightly smaller than the estimated error of the strain calculations, which is additional confirmation of the correctness of the error estimation by Kinaev *et al.* [1].

3.5. ε_{xx} strain field

The values of ε_{xx} were small over the whole observed area for all of the experiments as shown by the thin lines in Fig. 5a. In most cases ε_{xx} did not exceed 0.04. These small values were just above the measurement threshold. The HRR model also predicts small values of ε_{xx} as shown by the thick lines in Fig. 5a. Thus it can be concluded that there were no statistically significant discrepancies with the HRR model.

3.6. ε_{yy} strain field

The experimental ε_{yy} strain map for an applied stress intensity factor of K_I of 35 MPa $\sqrt{\text{m}}$ is presented in Fig. 5b. The experimental results, which are shown as thin lines are compared with theoretical predictions, shown as thick lines. This strain maps can be characterised as having "ridges" with high strain values extending in directions making angles of 60° with the overall direction of crack propagation. These strain ridges corresponded in direction to the direction of crack branching.

The measured isostrain contour corresponding to the value of 0.06 showed reasonable agreement between experiment and HRR prediction in the region ahead of the crack. However, there were significant differences between the experimental results and the HRR model. For example, in the upper half of the experimental strain map there were areas with strain values up to 0.18. These areas were roughly circular about 10 μm in diameter with centres located at the following coordinates: (1) $x = 12.5$ μm, $y = 20$ μm with strain values up to 0.18; (2) $x = 11$ μm, $y = 11$ μm, strain values more then 0.12; and (3) $x = 20$ μm, $y = 14$ μm, strain values more then 0.12. These areas showed more plasticity than predicted by HRR model. The difference between the experimental values and the HRR prediction at these areas was up to 0.08. This difference is higher than the accuracy of measurements ($\Delta\varepsilon = \pm 0.02$) and, hence, statistically meaningful. Furthermore, before these plasticity islands and in the same direction there was an area located at $x = 12$ μm, $y = 10$ μm where the strain was as low as 0.04. There was a similar area of extra plasticity in the lower half of the strain map located at (17.5 μm, -17.5 μm). Another difference between the experiment and the HRR model was in the position and shape of the area in the vicinity of the crack tip with strains of 0.12 and 0.18. Fig. 5b shows that these areas were displaced approximately 5 μm

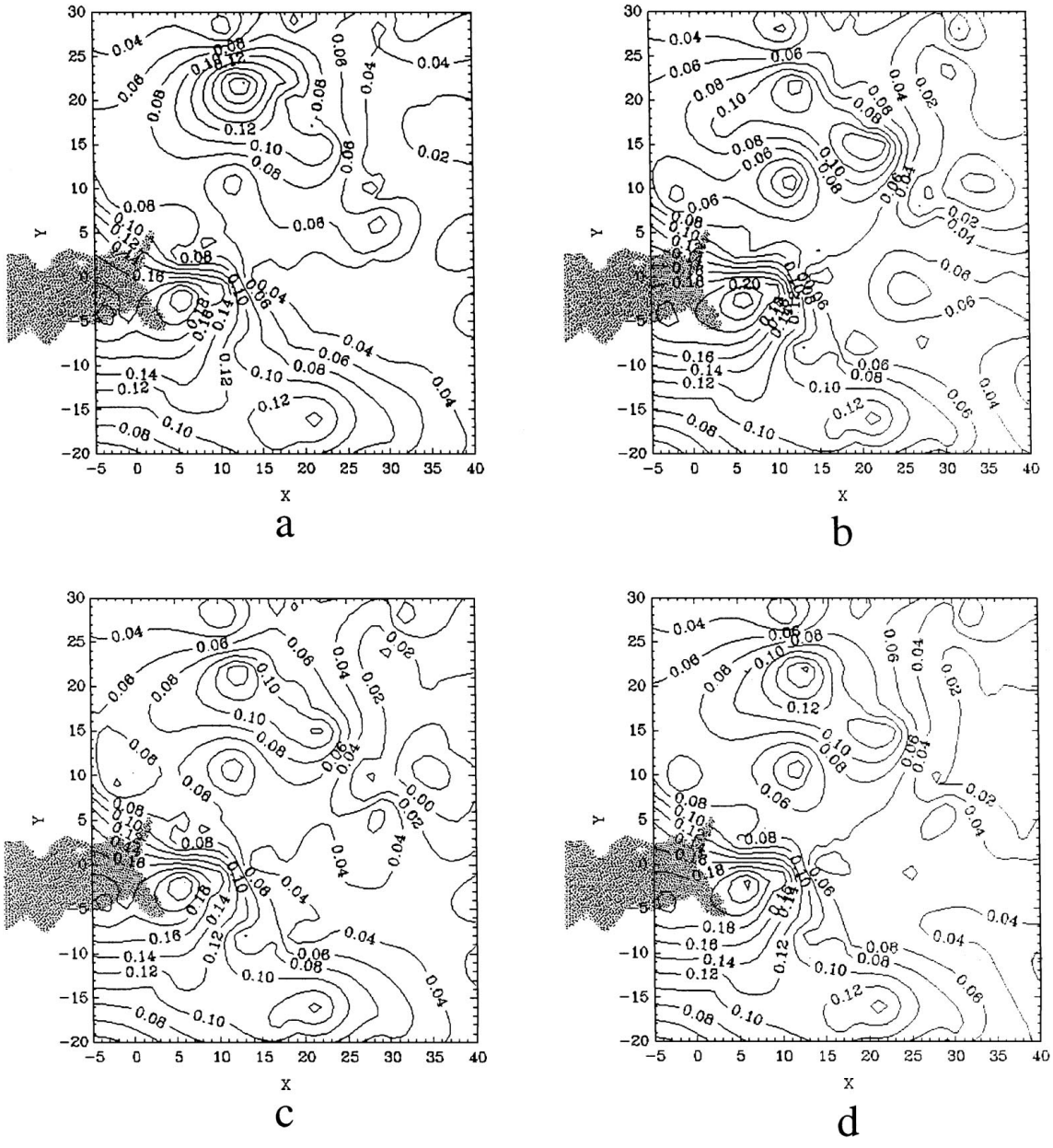

Figure 4 ε_{yy} strain distributions of at the crack tip at different time intervals after application an applied stress intensity factor K_I of 35 MPa $\sqrt{\text{m}}$: (a) 2 min after loading; (b) 30 min after loading; (c) 60 min after loading; (d) average over all 5 measurements at this value of K_I. Shading shows cross-sectional crack shape.

towards the lower part of the strain map. Their shape also differed from that expected for the HRR model. The HRR model predicts the shape of each isostrain contour to be double lobed. In contrast the experimental isostrain contour for ε_{yy} of 0.18 formed an elongated and relatively sharp ended area, with a center displaced approximately 5 μm in the negative Y-direction. Similarly, the isostrain contour for ε_{yy} of 0.12 could be considered as corresponding to only the lower lobe of the HRR model (Fig. 5a) whose center was displaced a distance of 5 μm in the negative Y-direction and approximately 2 μm in the positive X-direction. For the experiments carried out at the other stress intensity factors, the strain in the vicinity of the crack tip was also distributed asymmetrically.

Thus, the following conclusions could be drawn from the comparison of the experimentally measured ε_{yy} strain maps with the HRR predictions. (1) The scale of the features of the ε_{yy} strain field was consistent with HRR predictions. (2) In the most cases, the ε_{yy} strain field was asymmetric. (3) The shapes of the high ε_{yy} strain contours were in most cases more elongated than predicted by the HRR model. (4) There were islands with high values of ε_{yy} at distances of 20–25 μm from the crack tip.

3.7. γ_{xy} strain field

Fig. 5c shows that shear strains γ_{xy} were significantly higher than predicted by the HRR model. The shear strain distributions were not consistent with the HRR predictions and were different from experiment to experiment. For example, for the stress intensity factor of 35 MPa $\sqrt{\text{m}}$ (Fig. 5c) the shear strain formed a large peak in the bottom of the strain map near the crack tip area where the absolute values of the shear

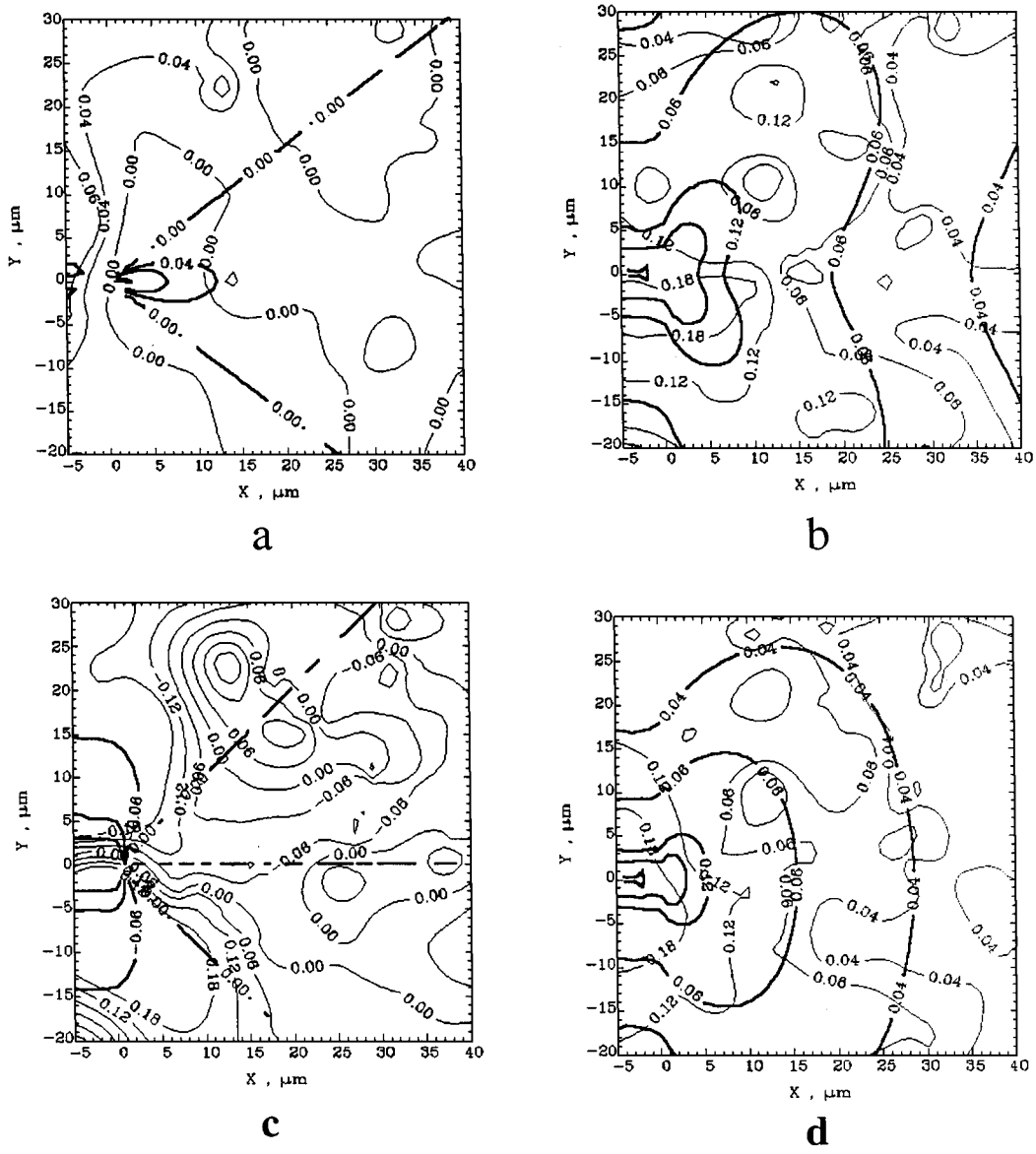

Figure 5 Measured crack tip strain distribution (thin lines) compared with predictions from HRR model (thick lines) for the applied stress intensity factor K_I of 35 MPa $\sqrt{\text{m}}$: (a) ε_{xx}; (b) ε_{yy}; (c) γ_{xy}; (d) 15 ε_{ef}.

strain was higher than 0.18, whereas the HRR model predicts for this area magnitudes of γ_{xy} not exceeding 0.06. For the stress intensity factor of 20 MPa $\sqrt{\text{m}}$ the γ_{xy} shear strain distribution had a maximum exceeding 0.18 in absolute value in an oval area in the crack tip region and the isostrain contour for γ_{xy} shear strain of 0.12 formed a pattern elongated in the crack direction. In contrast the HRR model predicts a considerably smaller shear deformation in this area. Thus, the γ_{xy} shear strain distribution was not consistent with HRR predictions.

3.8. Total effective strain ε_{ef}

Fig. 5d presents the comparison with the HRR model of the effective strain for the case of applied stress intensity factor K_I of 35 MPa $\sqrt{\text{m}}$. The isostrain contours for ε_{ef} of 0.04 and 0.06 were in a reasonable agreement with the HRR predictions for the area directly ahead of the crack tip, but not for regions sideways ahead of the crack. In the bottom and upper parts of the strain map, the measurements gave areas corresponding to ε_{ef} of 0.06 which were much further from the crack tip than the theoretical contours. Fig. 5d shows that the isostrain contour for ε_{ef} of 0.06 formed a double lobed shape which is different from the HRR predictions. Furthermore, the areas corresponding to ε_{ef} of 0.12 and 0.18 were larger than those predicted by the HRR model. These areas also were displaced towards the bottom of the strain map.

The total effective strain (in the crack growth direction) and the distance from the crack was normalised using the same procedure of McClung and Davidson [15]. The strain was normalised by the yield strain $\varepsilon_0 = \sigma_0/E$. The distance from the crack tip was normalised by the parameter $(K_I/\sigma_0)^2$. The normalised effective strain is presented in Fig. 6. The total effective strain for the experiments at a stress intensity factor of 35 MPa $\sqrt{\text{m}}$ was in good agreement with the HRR model in the area of reliable experimental data (at a phyisical distance greater then 4 μm from the crack tip or a normalised distance greater than 0.009).

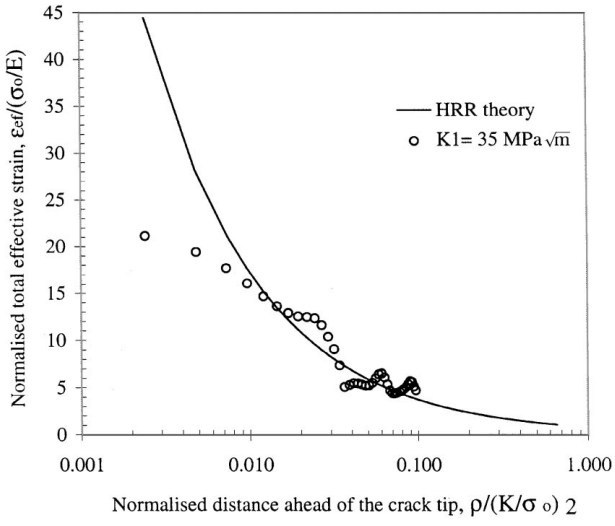

Figure 6 Distribution of the total effective strain ε_{ef} in the direction of crack propagation.

4. Discussion

4.1. Crack front profile

The measured crack front profile for the case of a stress intensity factor of 35 MPa $\sqrt{\text{m}}$ was close to an ideal crack front perpendicular to the external surface. Thus the measurements for this case should be close to the ideal case. In contrast, for the other values of stress intensity factor, the crack front was not perpendicular to the external surface, and consequently this non-ideal crack front may cause complications in the measured strain distributions. Consequently, in the evaluation of the results, most weight has been placed on the results for 35 MPa $\sqrt{\text{m}}$.

4.2. Crack branching

Significant crack branching was observed. The crack branches made an angle of about 60° with the direction of overall propagation of the fatigue precrack. The direction of crack branching was in the same direction as the major "ridges" of ε_{yy} strain, which in turn were in the same directions as predicted by the HRR model. Furthermore, the measured magnitudes of the ε_{yy} strain in this same direction were in general greater than the values predicted by the HRR model. It is expected that these phenomena are related.

4.3. Comparison with HRR

The following discrepancies between the measured strain fields for AISI 4340 and the HRR predictions are noteworthy. (1) The crack branching. (2) Values of CTOD significantly higher than predicted by HRR. (3) The major "ridge" of ε_{yy} strain an angle of about 60° with the direction of overall propagation of the fatigue precrack, in which the measured magnitudes of the ε_{yy} strain in were greater than the values predicted by the HRR model. (4) Asymmetric shape of the plastic zone as measured by the ε_{yy} strain. (5) Islands of extra ε_{yy} strain. (6) Values of shear strain γ_{xy} significantly higher than predicted by the HRR model.

These discrepancies might have arisen because the HRR model might not be appropriate for the material being studied or at the scale of this study. An alternative description of the strain field at the crack tip was recently proposed by Fleck and Hutchinson [17] based on strain gradient plasticity (SGP).

The asymmetric shape of the plastic zone could be attributed to a slight asymmetry in the loading geometry and/or local inhomogenities of the material. Indeed, even a small asymmetry in loading conditions might result in a preferential strain distribution.

A reason for such a disagreement with the theoretical prediction of the total effective strain might arise because the HRR model considers the material as homogeneous and isotropic. In our experiments the strain measurements were evaluated with a grid spacing of 3–6 μm. This scale is comparable with the grain size of the 4340. Therefore, the material could not be considered as homogeneous and isotropic. It means, that the shear strain might vary from grain to grain, depending on the crystallographic orientation of the grain.

4.4. Comparison with strain gradient plasticity theory

An alternative description of the strain field at the crack tip was recently proposed by Fleck and Hutchinson [17] based on strain gradient plasticity (SGP). Strain gradient plasticity assumes that the stress is increased by the gradient of the strain. Strain gradients can arise due to the geometry of the loading or/and due to plastic inhomogenities within the material (e.g. harder particles). There are significant strain gradients at a crack tip and consequently it is useful to evaluate the importance of strain gradient plasticity in our experiments. Strain gradient effects are expected to have a significant influence at a distance from the crack tip of the same order of magnitude as a characteristic material length l. However, currently, there is no theoretical way to evaluate this parameter from the first principles. Fleck and Hutchinson [17] showed that the value of l is approximately 5 μm for pure copper. When the strain gradient plasticity dominates, the following equation describes the strain field for the mode I loading [18, 19]:

$$\begin{bmatrix} \varepsilon_{\rho\rho} = -\varepsilon_{\theta\theta} \\ \varepsilon_{\rho\theta} \end{bmatrix} = \rho^{-\frac{n}{n+1}} \left(\frac{\sqrt{3}}{2}\right)^{n+1} \left(\frac{n+1}{n}\right)^{n} \times \left(\frac{B_I^{(o)^2}}{\sigma_0^2}\right)^{\frac{n-1}{2}} \frac{B_I^{(o)}}{\sigma_0} \begin{bmatrix} -\cos\frac{n+2}{n+1}\theta \\ \sin\frac{n+2}{n+1}\theta \end{bmatrix} \quad (8)$$

where $B_I^{(o)}$ is the parameter representing the amplitude of the stress, similar to the stress intensity factor. This parameter is related to the stress intensity factor K_I by [19]:

$$\sqrt{B_I^{(o)^2} + \frac{A_I^{(o)^2}}{2(1-\nu)(3-2\nu)l}} = \frac{K_I}{\sqrt{2\pi}} \frac{1}{\sqrt{3-2\nu}} \quad (9)$$

where $B_I^{(o)}$ and $A_I^{(o)}$ are the stress and couple stress amplitudes, ν is the Poisson's ratio and l is the intrinsic material length.

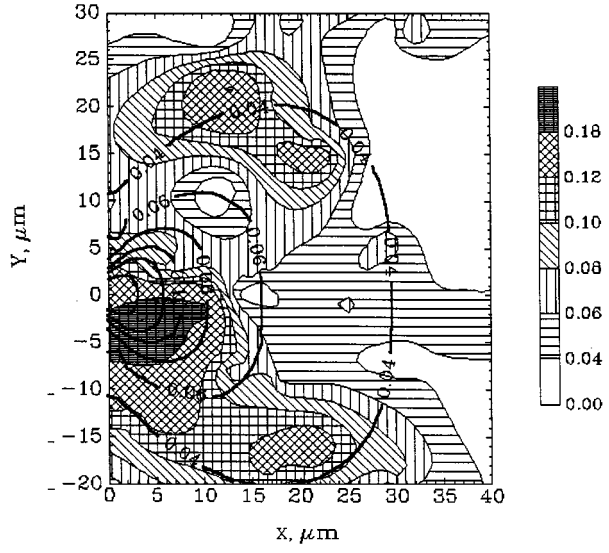

Figure 7 Measured crack tip ε_{yy} strain distribution (filled map) compared with the theoretical predictions (thick lines) for the SGP model.

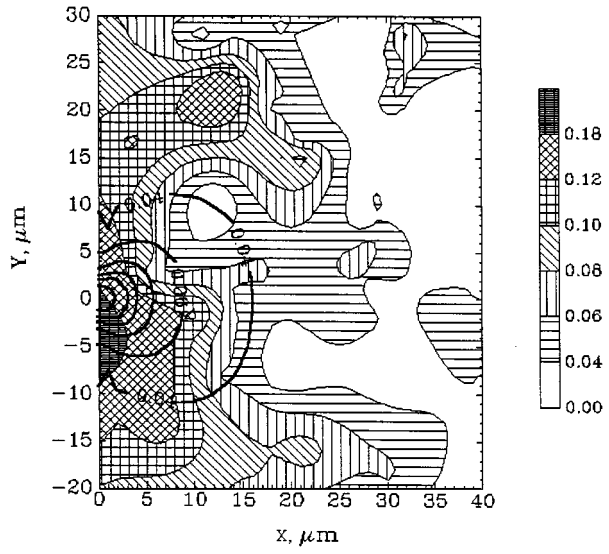

Figure 8 Measured crack tip total effective strain ε_{ef} distribution (filled map) compared with the theoretical predictions (thick lines) for the SGP model.

Because techniques for the theoretical evaluation of material intrinsic parameter l, the stress amplitude $B_I^{(o)}$ and couple amplitude $A_I^{(o)}$ from the stress intensity factor have not been reported in the literature, these parameters were determined by linear least squares fitting of the SGP model and the experimental results. Equation 9 indicates that it is not possible to separate the couple amplitude $A_I^{(o)}$ and the material intrinsic parameter l, so their ratio $A_I^{(o)}/l$ was evaluated. For every ith data point the difference δ between the measured and calculated values of ε_{yy} was determined using

$$\delta_i = \left(\varepsilon_{yy}^{i,\text{exp}} - \varepsilon_{yy}^{i,\text{calc}}\right)^2, \tag{10}$$

where $\varepsilon_{yy}^{i,\text{exp}}$ is the measured value of ε_{yy} for the ith data point and $\varepsilon_{yy}^{i,\text{calc}}(B_I^{(o)},\ A_I^{(o)}/l)$ is the calculated value of ε_{yy} for the ith data point, dependent on the parameters to be evaluated. The sum $\sum_{i=1}^{N}\delta_i$ was minimized whilst satisfying Equation 9 for the value of the applied stress intensity factor K_I of 35 MPa $\sqrt{\text{m}}$. The best results were achieved for $B_I^{(o)} = 8.88$, $A_I^{(o)}/l = 0.3$. The measured and calculated strain fields for ε_{yy} and total effective strain ε_{ef} are presented in Figs 7 and 8. The HRR model provides significantly better agreement than SPG in both the plastic zone shape and size. This provides an experimental basis for the conclusion that the intrinsic length for 4340 is smaller than about 5 μm. Thus the SGP model is not applicable for the description of the strain distribution for 4340.

5. Conclusions

- The strain maps in the crack tip area has been measured for AISI 4340 high strength steel.
- No significant creep was observed.
- The measured values of CTOD were greater than expected from the HRR model.
- Crack tip branching was observed in every experiment. The direction of crack branching was in the same direction as a major "ridge" of ε_{yy} strain, which in turn was in the same direction as predicted by the HRR model. Furthermore, the measured magnitudes of the ε_{yy} strain in this same direction were in general greater than the values predicted by the HRR model. This indicates more plasticity in the crack tip region than expected from the HRR model. This greater plasticity could be related to the larger than expected CTOD values.
- The following discrepancies between the measured strain fields for AISI 4340 and the HRR predictions are noteworthy. (1) The crack branching. (2) Values of CTOD significantly higher than predicted by HRR. (3) The major "ridge" of ε_{yy} strain an angle of about 60° with the direction of overall propagation of the fatigue precrack, in which the measured magnitudes of the ε_{yy} strain in were greater than the values predicted by the HRR model. (4) Asymmetric shape of the plastic zone as measured by the ε_{yy} strain. (5) Islands of extra ε_{yy} strain. (6) Values of shear strain γ_{xy} significantly higher than predicted by the HRR model.

Acknowledgement

This work was supported by the Australian Research Council.

References

1. N. N. KINAEV, D. R. COUSENS and A. ATRENS, The Crack Tip Strain Field of AISI, Part I: Measurement Technique, *J. Mater. Sci.* **34** (1999) 4909.
2. N. N. KINAEV, D. R. COUSENS and A. ATRENS, The Crack Tip Strain Field of AISI, Part III: Comparison with Theoretical Models, *J. Mater. Sci.* **34** (1999) 4931.
3. R. M. RIECK, A. ATRENS and I. O. SMITH, *Met. Trans.* **20A** (1989) 889–895.
4. A. ATRENS, C. C. BROSNAN, S. RAMAMURTHY, A. OEHLERT and I. O. SMITH, *Measurement Science and Technology* **4** (1993) 1281–1292.
5. S. RAMAMURTHY and A. ATRENS, *Corrosion Science* **34** (1993) 1385–1402.
6. A. OEHLERT and A. ATRENS, *Acta Metallurgica et Materialia* **42** (1994) 1493–1508.
7. J. W. HUTCHINSON, *J. Mech. Phys. Solids* **16** (1968) 13–31.

8. *Idem., ibid.* **16** (1968) 337–347.
9. J. R. RICE and G. F. ROSENGREN, *ibid.* **16** (1968) 1–12.
10. C. F. SHIH, "Tables of Hutcinson-Rice-Rosengren Singular Field Quantities," Brown University, USA, 1983.
11. G. HAN, M. A. SUTTON and Y. J. CHAO, *J. Exp. Mechanics* (1994) 125–140.
12. M. S. DADKHAH and A. S. KOBAYASHI, in "Advances in Fracture Research," Proceedings of the 7th International Conference on Fracture (ICF7) (Pergamon, Oxford, UK, 1989) Vol. 1, pp. 689–704.
13. F. P. CHIANG and T. V. HAREESH, *Int. J. Fracture* **36** (1988) 243–257.
14. L. ALLAIS, M. BORNERT, T. BERTHEAU and D. CALDEMAISON, *Acta Metall. Mater.* **42** (1994) 3865–3880.
15. R. C. MCCLUNG and D. L. DAVIDSON, *Eng. Fract. Mech*, **39** (1991) 113–130.
16. J. W. DALLY and W. F. RILEY, "Experimental Stress Analysis" (McGaw-Hill, 1965) p. 34.
17. N. A. FLECK, N. A. and J. W. HUTCHINSON, *J. Mech. Phys. Solids* **41** (1993) 1825–1857.
18. Y. HUANG, L. ZHANG, T. F. GUO and K. C. HWANG, "Advances in Fracture Research, ICF9" (1997) pp. 2275–2286.
19. Y. HUANG, L. ZHANG, T. F. GUO and H. C. HWANG *J. Mech. Phys. Solids* **45** (1998) 439–65.

Received 25 November 1998
and accepted 15 March 1999